Improved Iron Loss Prediction Models for Interior PMSMs Considering Coupling Effects of Multiphysics Factors

Lin Liu, *Student Member, IEEE*, Xin Ba*, Youguang Guo, *Senior Member, IEEE*, Gang Lei, *Member, IEEE*, Xiaodong Sun, *Senior Member, IEEE*, and Jianguo Zhu, *Senior Member, IEEE*

***Abstract*—This paper presents improved iron loss analytical prediction models for interior permanent magnet synchronous motors (IPMSMs) used in electric vehicles. The effects of slotting harmonics, pulse-width modulation (PWM) carrier harmonics, temperature rise and mechanical stress are considered in the proposed models. Specifically, by investigating the stator flux density as piecewise linear with trapezoidal waveform, the iron losses in the teeth and yoke regions are calculated separately, considering the different magnetic field distributions and waveforms. To deliberate the PWM harmonic influence, a correction coefficient is added to the hysteresis loss models, while the eddy current loss models are updated by summing all the eddy current losses caused by the power supplying current harmonics. Moreover, the coupling interaction effects of magnetic, thermal, and stress fields on the empirical coefficients of hysteresis and eddy current losses are analyzed in detail and also implemented in the iron loss prediction process. The feasibility and superiority of the proposed models are verified by numerical and experimental case studies on an IPMSM prototype.**

***Index Terms*—Electric vehicles, electrical machines, interior permanent magnet synchronous motor (IPMSM), iron loss, harmonics, pulse width modulation (PWM), multiphysics.**

I. Introduction

Concerns on global fossil fuel shortage and automobile emissions have contributed to the increasing investment and application

This work was supported in part by the Australian Research Council under Discovery Grants DP120104305 and DP180100470, and the Foundation of China Scholarship Council under Grant 201906730038.

L. Liu, X. Ba, Y. Guo, and G. Lei are with the School of Electrical and Data Engineering, University of Technology Sydney, NSW 2007, Australia (e-mails: Lin.Liu@student.uts.edu.au; Xin.Ba@student.uts.edu.au; Youguang.Guo-1@uts.edu.au; Gang.Lei@uts.edu.au).

X. Sun is with the Automotive Engineering Research Institute, Jiangsu University, Zhenjiang 212013, China (e-mail: xdsun@ujs.edu.cn).

J. Zhu is with the School of Electrical and Information Engineering, The University of Sydney, NSW 2006, Australia (e-mail: jianguo.zhu@sydney.edu.au).

Corresponding author: Dr. Xin Ba (Postal address: CB11.08.305, 81 Broadway, Ultimo, NSW, 2007 Australia; Phone: +61 2 9514 2650)

of electric vehicles (EVs). The topology of interior permanent magnet synchronous motor (IPMSM) has been considered as suitable for driving EVs under complex operating conditions, thanks to its advantages in the areas of weight and space saving, efficiency improvement, speed range expansion as well as control performance promotion [1]-[4]. However, the iron loss of IPMSMs can be significantly interfered by the time-varying working conditions and coupling effects of multiphysics factors like magnetic, thermal and mechanical stress field distributions [5], [6]. Moreover, the harmonics of non-sinusoidal magnetic flux in the motor stator, caused by both stator slotting structure and pulse-width modulation (PWM) inverter, would result in additional iron loss [7], [8].

In this case, the development of an accurate iron loss calculation technique, as a prerequisite for the design and optimization of IPMSMs in EVs, has attracted great research interests from academia and industry worldwide. Recently, the finite element analysis (FEA) based on the well-known Bertotti model has shown satisfactory performances for calculating iron loss with reasonable accuracy. In [9], the FEA was utilized to predict the iron loss and the magnet eddy current loss of permanent magnet synchronous machines (PMSMs) with concentrated windings. In [10], [11], the iron loss calculation models accounting simultaneously for magnetic hysteresis and eddy currents were investigated for steel laminations at high frequencies by using the FEA method. In [12], the influence of iron loss on IPMSM electromagnetic characteristics was evaluated based on the inverse solution of the flux linkages extracted via FEA. In [13], the iron loss caused by fringing fluxes in an axial-flux PMSM was calculated through FEA. Although the FEA can estimate iron losses conveniently for nonlinear problems with complex structures, it is time-consuming, which poses a great difficulty to design optimization process of PMSM with a large number of iterations. Moreover, the impacts of multiphysics factors such as temperature and stress on motor performance cannot be easily distinguished via FEA. It is therefore strongly desired to develop iron loss calculation methods that cannot only greatly shorten the calculation time, but also indicate the interactions of motor parameters, while maintaining the calculation accuracy.

To reduce the computational cost, alternative iron loss calculation methods based on analytical models were proposed. For instance, the magnetic equivalent circuit (MEC), as a promising analytical method, has been applied to estimate the iron loss and analyze the operating performance as well as the relationship between static and dynamic flux densities for various electrical machines [14]-[17]. However, the MEC calculation accuracy might be discounted since this method prefers the average core magnetic density to harmonic component, without giving enough considerations of the iron loss from harmonics contribution. Meanwhile, in EVs, it is impractical for a drive motor to work only under definite and standard conditions. Non-sinusoidal flux density waveforms with rich harmonics can impact significantly on iron loss characteristics.

According to the sources, there exist two types of flux density harmonics: the spatial harmonics due to stator slotting and the carrier harmonics generated by the PWM inverter. To reveal the influences of harmonics, analytical iron loss models are investigated by taking into account both the spatial and carrier harmonics. In [18] and [19], an analytical iron loss calculation method was proposed for a spoke-type in-wheel PMSM with the bridge saturation and magnetic field harmonics. In [20], aiming at the influence of harmonics, an analytical iron loss calculation method was proposed for an integer-slot IPMSM during flux weakening, in which a harmonic loss voltage and a harmonic loss coefficient were added to the iron loss resistance model. The

relationship between the harmonic additional loss and the harmonic voltage was analyzed. Experimental results reported in [21] indicates that the iron losses of electrical machines fed by PWM inverters could be almost three times higher than those fed by the ideal sinusoidal currents. Similar results were also reported in [22]-[25].

The abovementioned studies have shown successful progress in improving the speed and accuracy of iron loss prediction in electrical machines in the presence of either spatial or carrier harmonics. However, in the presence of both spatial and carrier harmonics, substantial work is still needed to improve the analytical iron loss prediction model. Furthermore, since the magnetic properties including iron losses are susceptible to temperature and mechanical stress [27]-[28], the interaction of multiphysics effects, such as thermal and stress characteristics, also need to be considered to improve the iron loss prediction accuracy for the design and optimization of PMSMs.

To address the above-mentioned issues, this paper proposes an improved analytical iron loss prediction model for IPMSMs utilized as the drive motor of EVs. The novelty is mainly manifested in that the influences of different physical factors including both the spatial harmonics from slotting and carrier harmonics due to PWM inverter, the temperature and compressive stress on iron loss are fully considered in the proposed analytical models. The prediction accuracy can be improved while the computational burden is reduced. The remainder of this paper is organized as follows. Section II describes the principles of the proposed iron loss prediction model. In Section III, an IPMSM prototype is employed for the case studies. The coupling effects of multiphysics factors are also analyzed by the finite element method (FEM). Then, the iron loss of the EV IPMSM prototype is calculated. The effectiveness and superiority of the proposed method are verified through a comparative analysis of the numerical and experimental results, as presented in Section IV. Finally, conclusions are drawn in Section V.

II. Problem Formulation and Models

Classically, Bertotti's iron loss separation model, consisting of hysteresis loss density P_h, eddy current loss density P_e and additional loss density P_{ad}, has been commonly employed for calculating iron loss density in silicon steel sheets. Under sinusoidal magnetization, the total iron loss density P_{total} in a silicon steel sheet sample can be calculated by [8]

$$P_{total} = P_h + P_e + P_{ad} \tag{1}$$

with

$$\begin{cases} P_h = K_h \dfrac{\omega_s}{2\pi} B_m^{\alpha} \\ P_e = \dfrac{d^2}{12\eta_{Fe}\rho_{Fe}} \dfrac{1}{T}\int_0^T \left(\dfrac{dB(t)}{dt}\right)^2 dt = K_e \dfrac{1}{T}\int_0^T \left(\dfrac{dB(t)}{dt}\right)^2 dt \\ P_{ad} = \dfrac{\sqrt{\sigma_{Fe} GVS}}{\rho_{Fe}} \dfrac{1}{T}\int_0^T \left|\dfrac{dB(t)}{dt}\right|^{3/2} dt = K_{ad} \dfrac{1}{T}\int_0^T \left|\dfrac{dB(t)}{dt}\right|^{3/2} dt \end{cases} \tag{2}$$

where ω_s is the motor angular frequency, B_m the amplitude of the magnetic flux density, d the thickness of silicon steel sheet, S the cross-sectional area of the iron core, G=0.1375 a dimensionless constant, $\sigma_{Fe}=1/\eta_{Fe}$ the conductivity, V a parameter characterizing the statistical distribution of local coercive fields, T the excitation period. η_{Fe} and ρ_{Fe} are the resistivity and density of core material,

respectively. K_h and α are both hysteresis loss empirical coefficients, and $1.8 \le \alpha \le 2.2$. $K_e = d^2/(12\eta_{Fe}\rho_{Fe})$ is defined as the eddy current loss coefficient while $K_{ad} = \sqrt{\sigma_{Fe} GVS}/\rho_{Fe}$ is set as the additional loss coefficient.

Since the additional loss generally accounts for only a small percentage of the total iron loss [5], [26], it is ignored in the iron loss calculation, and according to (2), the accurate estimation of magnetic field and coefficients K_h and K_e is crucial for calculating iron loss.

A. Iron Loss Considering Slot Harmonics

Unlike the ideal case of iron loss estimation in a silicon steel sheet sample under sinusoidal magnetization, the calculation of iron loss in a PMSM must consider both the fundamental and harmonic flux density waveforms. While there exist two types of harmonics, this subsection calculates the iron loss by taking into account the spatial harmonics due to the stator slotting and rotor structure. To consider the effects of spatial harmonics, the stator is divided into the tooth and yoke regions. The hysteresis and eddy current losses in each region are predicted separately with consideration of non-sinusoidal flux density waveforms.

i) Iron Loss Model of Tooth Region

The hysteresis loss equals the area enclosed by the quasi-static hysteresis loop, which is mainly related to the fundamental frequency of magnetic flux density, temperature rise and compressive stress instead of the waveform harmonics. In contrast, the eddy current loss highly depends on the waveform harmonics, and to calculate the eddy current loss, the harmonics of non-sinusoidal flux density waveforms must be considered [7], [18]-[19]. Because of the complexity of harmonic evaluation process, by using FEM, the tooth flux density waveform is transformed into piecewise linear or trapezoidal waveform, as shown in Fig. 1. Under the magnetization of trapezoidal waveform, the eddy current loss density of the tooth can be calculated as [29]

$$P_e = K_e \frac{1}{T} \sum_{i=1}^{N_{Li}} \int_{t_{i-1}}^{t_i} \left(\frac{dB_i(t)}{dt}\right)^2 dt \tag{3}$$

where N_{Li} is the number of linear intervals.

For the tooth region, the non-dominant longitudinal component of flux density can be ignored [29], and the time required for a magnet to pass a slot pitch can be expressed as

$$\Delta t = \frac{T}{2} \frac{1}{N_R N_S} \tag{4}$$

where N_R and N_S are the numbers of phases and slots per pole per phase of the PMSM, respectively.

For a trapezoidal waveform, the changing rate of flux density with respect to time can thus be transformed into

$$\frac{dB_T(t)}{dt} = \frac{B_{Tm}}{\Delta t} \tag{5}$$

As shown in Fig. 1, the mutation of flux density change rate happens four times in one excitation period. In this case, based on (3), the eddy current loss density in the tooth region can be expressed by

$$P_{eT} = K_e \frac{4}{T} \left(\frac{B_{Tm}}{\Delta t}\right)^2 \Delta t \tag{6}$$

Substituting Δt of (4) into (6), one obtains

$$P_{eT} = 8K_e N_R N_S \left(\frac{B_{Tm}}{T}\right)^2 \tag{7}$$

The iron loss in the tooth region can be calculated by

$$P_{totalT} = P_{hT} + P_{eT} = K_h \frac{\omega_s}{2\pi} B_{Tm}^{\alpha} + 8K_e N_R N_S \left(\frac{B_{Tm}}{T}\right)^2 \tag{8}$$

where P_{totalT} and P_{hT} are the total iron loss density and hysteresis loss density in the tooth region, respectively.

ii) Iron Loss Model of Yoke Region

In this subsection, the flux densities in the yoke region are also considered as piecewise linear with trapezoidal waveform obtained by using FEM, as shown in Fig. 2. However, the calculation of the yoke iron loss density is not the same as that for the tooth region, which should be estimated separately with both longitudinal and normal components. Moreover, although the rise and fall times of flux density in the yoke are independent of the position along the radial direction, the amplitude of flux density normal component depends highly on the position [29]. Thus, the eddy current loss models of yoke region are derived under longitudinal and normal components, respectively.

To calculate the eddy current loss due to the longitudinal component, a quantity

$$\beta = \frac{pW_m}{2\pi r} \tag{9}$$

is defined to represent the coverage of the width of magnet, where p is the number of poles, W_m the effective width of magnet for the V-shaped IPMSM, and r the rotor outer radius.

The time required by a magnet to rotate from one point to another in the yoke can be expressed as

$$\Delta t_1 = \frac{W_m}{r\omega_{mech}} \tag{10}$$

where ω_{mech} is the motor mechanical speed and $\omega_{mech}=2\omega_s/p$.

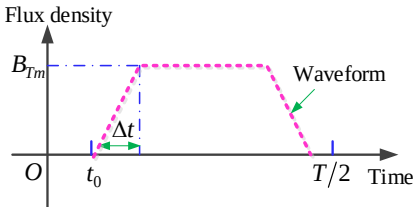

Fig. 1. Flux density waveform in the tooth region.

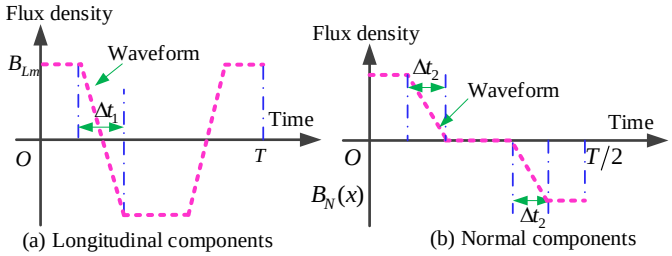

Fig. 2. Flux density waveforms in the yoke region.

Substituting (9) into (10), one obtains

$$\Delta t_1 = \frac{\beta\pi}{\omega_s} \tag{11}$$

During Δt_1, as shown in Fig. 2(a), the variation of longitudinal flux density is $2B_{Lm}$, and

$$\frac{dB_L(t)}{dt} = \frac{2B_{Lm}}{\Delta t_1} = \frac{2\omega_s B_{Lm}}{\pi\beta} \tag{12}$$

This change happens twice during an excitation period. Substituting B_L in (12) as B_i in (3), one obtains the average eddy current loss density in the yoke due to the change of longitudinal flux density as

$$P_{eYL} = 8K_e \frac{\omega_s B_{Lm}^2}{\pi\beta T} \tag{13}$$

The eddy current loss due to the varying normal component of flux density is also estimated. Fig. 2(b) shows the normal component of flux density waveform in the yoke, where $B_N(x)$ is the magnitude of normal component at distance x from the outer edge of the yoke. By employing the theoretical quadric fitting method [29], $B_N(x)$ can be expressed as

$$B_N(x) = (ax + bx^2)B_{Lm} \tag{14}$$

where a and b are the fitting coefficients.

The time required by a magnet to rotate for one slot pitch can be calculated by

$$\Delta t_2 = \frac{\Delta x}{r\omega_{mech}} \tag{15}$$

$$\Delta x = \frac{2\pi r}{pN_S} \tag{16}$$

where N_S is the number of slots per pole per phase.

During this time period, the flux density normal component varies linearly with the amount of $B_N(x)$, and can be noted as $B_N(x,t)$. The variation rate of normal component is calculated by

$$\frac{\partial B_N(x,t)}{\partial(t)} = \frac{N_S}{\pi}\omega_s B_N(x) \tag{17}$$

Combining (3), (15), (16) and (17), one can obtain the eddy current loss density due to the flux density normal component at point x as

$$P_N(x) = 4K_e \frac{N_S\omega_s}{\pi T}\left[B_N(x)\right]^2 \tag{18}$$

By integrating $P_N(x)$ over x, the average loss density due to the normal component can be obtained as

$$P_{eYN} = C_N \cdot 4K_e \frac{N_S\omega_s}{\pi T} B_{Lm}^2 \tag{19}$$

where

$$C_N = \frac{a^2}{3} + \frac{ab}{2} + \frac{b^2}{5} \tag{20}$$

The total iron loss in the yoke region can be obtained as

$$\begin{aligned} P_{totalY} &= P_{hY} + P_{eYL} + P_{eYN} \\ &= K_h \frac{\omega_s}{2\pi} B_{Lm}^{\alpha} + 8K_e \frac{\omega_s B_{Lm}^2}{\pi\beta T} + C_N \cdot 4K_e \frac{N_S\omega_s}{\pi T} B_{Lm}^2 \end{aligned} \tag{21}$$

Finally, by multiplying the total iron loss densities of the tooth and yoke by the corresponding volumes, the total stator iron loss can be estimated as

$$P_{iron\_1} = P_{totalT}V_T + P_{totalY}V_Y \tag{22}$$

where V_T and V_Y are the tooth and yoke volumes, respectively.

B. Iron loss considering PWM carrier harmonics

The iron loss prediction model shown in (22) can account for the effects of magnetic field spatial harmonics and distribution, but it is derived under the assumption that the motor is driven by sinusoidal current input. However, the drive motors for EV are supplied by inverters and operate for a wide range of speed and torque, which generates extra iron loss due to the carrier harmonics.

As shown in Fig. 3, the distorted current injected by the inverter can produce minor hysteresis loops and generate additional hysteresis loss. Additional eddy current loss can also be produced by the flux density harmonics caused by the PWM carrier. To describe the effects of PWM carrier harmonics on iron loss prediction, an improved model is applied. A coefficient k_{h_PWM} is introduced to revise the calculation equations of hysteresis loss while the models of eddy current loss are updated by summing all the eddy current losses caused by harmonics, as given below [24], [30].

$$\begin{cases} P_{h\_PWM} = k_{h\_PWM} P_h \\ P_{e\_PWM} = \sum P_{e\_PWM}(n) \end{cases} \tag{23}$$

$$k_{h\_PWM} = 1 + C_h \frac{1}{B_m} \sum_{a=1}^{N} \Delta B_a \tag{24}$$

where P_{h_PWM} and P_{e_PWM} are the hysteresis and eddy current losses considering PWM carrier harmonics. $P_{e\_PWM}(n)$ is the eddy current loss caused by the n^{th} PWM harmonic, C_h the constant coefficient between 0.6 and 0.7 which depends on the lamination properties, and ΔB_a denotes the fluctuation in motor flux density, as seen in Fig. 3.

In the above-mentioned model, $P_{e\_PWM}(n)$ can be estimated from the flux density harmonics. According to the Faraday's law, the relationship between the supply voltage and flux density can be expressed as

$$u(t) = N_W S \frac{dB}{dt} \tag{25}$$

where N_W is the number of winding turns.

Assuming that the output voltage of the PWM inverter, marked as $v(t)$, is a periodic function, the stator terminal voltage can be expressed as (26) by using Fourier decomposition [23].

$$\begin{aligned} v(t) &= \sum_{n}^{\infty} V_n \cos 2n\pi ft \\ &= V_0 + V_1 \cos \omega_s t + V_2 \cos 2\omega_s t + V_3 \cos 3\omega_s t + \cdots \end{aligned} \tag{26}$$

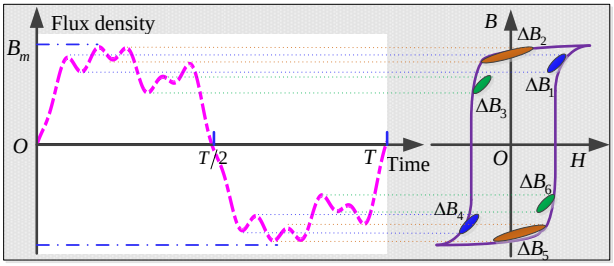

Fig. 3. Distorted flux density waveform with PWM inverter supply.

If the PWM inverter is well controlled, the positive and negative parts of the PWM waveform are symmetrical. No direct current component and even-order harmonics exist, and (26) can be transformed into

$$v(t) = V_1 \cos 2\pi ft + \sum_{n=3,5,7,\cdots}^{\infty} V_n \cos 2n\pi ft \tag{27}$$

where f is the fundamental frequency of the PWM waveform.

Substitute (27) into (25). After integration, the expression of magnetic flux density can be illustrated via

$$B(t) = \frac{1}{N_W S}\left(\sum_{n=1,3,5,\cdots}^{\infty} \frac{V_n}{2n\pi f} \sin 2n\pi ft \right) \tag{28}$$

Thus, the magnitude of the n^{th} harmonic of flux density is

$$B_{mn} = \frac{1}{N_W S} \frac{V_n}{2n\pi f} \tag{29}$$

where V_n is the magnitude of the n^{th} harmonic voltage, and can be estimated from the magnitude of fundamental voltage V_1 by [21]

$$\begin{cases} V_n = \dfrac{4J_h\left(\dfrac{\gamma k\pi}{2}\right)}{k\pi\gamma} V_1 \\ n = k\varepsilon \pm h \\ \text{while } k = 1,3,5\cdots, \quad h = 3(2j-1)\pm 1,\ j = 1,2,3\cdots \\ \text{while } k = 2,4,6\cdots, \quad h = \begin{cases} 6j+1,\ j = 0,1 \\ 6j-1,\ j = 1,2,\cdots \end{cases} \end{cases} \tag{30}$$

where J_h is the Bessel function, γ the modulation ratio, and ε the carrier ratio.

To reduce the computing burden, the Bertotti model is employed to predict the additional eddy current loss density due to the n^{th} carrier harmonic, as the following

$$P_{e\_PWM}(n) = K_e B_{mn}^2 f_n^2 = K_e \left(\frac{1}{N_W S} \frac{V_n}{2n\pi f}\right)^2 f_n^2 = K_e \left(\frac{1}{2\pi N_W S}\right)^2 V_n^2 \tag{31}$$

where f_n is the frequency of the n^{th} harmonic. Combining (8), (21), (22), (23), (24) and (31), the iron loss model in the presence of non-sinusoidal magnetic flux density and PWM carrier harmonics can be obtained as

$$P_{iron\_2} = \left(k_{h\_PWM}^T P_{hT} + P_{eT}\right) V_T + \left(k_{h\_PWM}^Y P_{hY} + P_{eYL} + P_{eYN}\right) V_Y + \left[K_e \left(\frac{1}{N_W S}\right)^2 \sum_{i=3,5,7\ldots}^{n} \left(\frac{V_n}{2\pi}\right)^2 \right] (V_T + V_Y) \tag{32}$$

C. Iron loss considering Multiphysics Factors

To incorporate multiphysics uncertainties including thermal and stress effects, the iron loss model of (32) is updated.

i) Iron Loss with Thermal Effect

Since core materials are sensitive to temperature, the influence of temperature should be reflected on iron loss. It is well known that the temperature effect mainly acts on the material resistance that is proportional to its length L, and inversely proportional to its cross-sectional area A_{CS}, namely,

$$R = \frac{\eta(T_{\circ C})L}{A_{CS}} \tag{33}$$

where R is the resistance of the material, and $\eta(T_{\circ C})$ is the material resistivity varying with temperature $T_{\circ C}$.

Therefore, both K_h and K_e are related to $T_{\circ C}$, or

$$\begin{cases} K_h = K_h(T_{\circ C}) \\ K_e = K_e(T_{\circ C}) = \dfrac{d^2}{12\eta_{Fe}(T_{\circ C})\rho_{Fe}} \end{cases} \tag{34}$$

According to the theory of linear relationship, $\eta_{Fe}(T_{\circ C})$ can be estimated by

$$\eta_{Fe}(T_{\circ C}) = \eta_{Fe}^0(1+\mu_T \Delta T_{\circ C}) \tag{35}$$

where η_{Fe}^0 is the equivalent resistivity of materials at the room temperature, μ_T the temperature coefficient obtained by fitting the iron loss curve under different temperatures, and $\Delta T_{\circ C}$ the temperature variation.

ii) Iron Loss with Stress Effect

Apart from the temperature effect, the remaining stress in silicon steel sheet, caused by punching, cutting and pressing, etc., is another important motivating factor responsible for the performance degradation, which would induce the enhancement of iron loss due to the newly arranged internal magnetic domain. To update the stress effect, the iron loss coefficients K_h and K_e should also be functions of stress, and can be noted as $K_h(\sigma)$ and $K_e(\sigma)$.

iii) Correlation Analysis

In order to simplify the fitting process of iron loss coefficients, the Pearson correlation analysis method is employed to analyze the relationship between iron loss coefficients and multiphysics factors. The Pearson correlation coefficient R_{XY} is defined as [5]

$$R_{XY} = \frac{\sum_{i=1}^{n}\left(X_i - \bar{\boldsymbol{X}}\right)(Y_i - \bar{\boldsymbol{Y}})}{\sqrt{(X_i - \bar{\boldsymbol{X}})^2 (Y_i - \bar{\boldsymbol{Y}})^2}} \tag{36}$$

where $\boldsymbol{X}=\{X_i;\ i=1,\cdots N\}$ is the set of input variables, $\boldsymbol{Y}=\{Y_i;\ i=1,\cdots N\}$ the set of corresponding output variables, and $\bar{\boldsymbol{X}}$ and $\bar{\boldsymbol{Y}}$ are the means of $\boldsymbol{X}$ and $\boldsymbol{Y}$, respectively.

Moreover, the closer R_{XY} is to 1, the stronger the correlation between the input and output variables. By taking advantage of the FEM data, the Pearson correlation coefficients between the iron loss coefficients, K_h and K_e, and the multiphysics factors at different operating speeds (from 500 rpm to 5500 rpm) are obtained, as shown in Fig. 4.

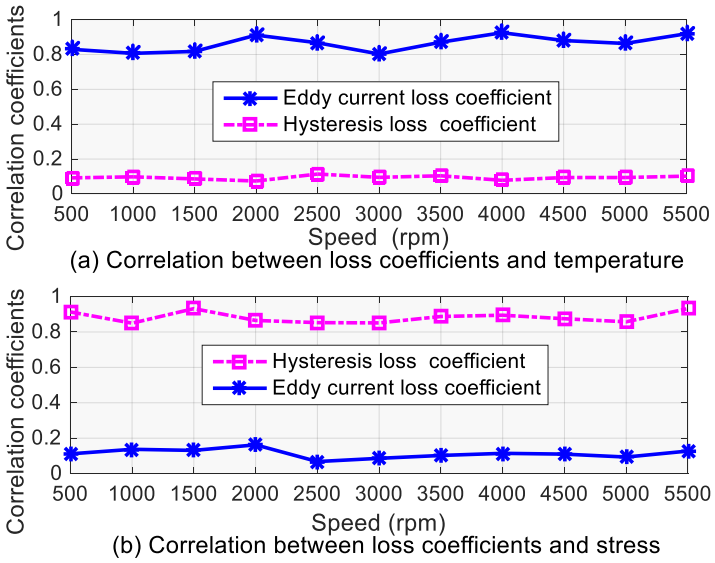

Fig. 4. Correlations between K_h and K_e with temperature and stress.

It can be concluded that the hysteresis loss coefficient has a strong relationship with the stress, while the eddy current loss coefficient significantly depends on the temperature. Finally, the proposed iron loss model considering the coupling effects of multiphysics factors can be summarized as

$$\begin{aligned} P_{iron\_2} = & \left(\frac{k_{h\_PWM}^{T} K_h(\sigma) \omega_s}{2\pi} B_{Tm}^{\alpha} + 8K_e(T_{\circ C}) N_R N_S (\frac{B_{Tm}}{T})^2 \right) V_T \\ & + \left\{ \frac{k_{h\_PWM}^{Y} K_h(\sigma) \omega_s}{2\pi} B_{Lm}^{\alpha} + \frac{4K_e(T_{\circ C}) \omega_s (2+\beta C_N N_S)}{\pi T \beta} B_{Lm}^{2} \right\} V_Y \\ & + \left\{ \frac{K_e(T_{\circ C})}{(N_W S)^2} \sum_{i=3,5,7...}^{n} \left(\frac{V_n}{2\pi} \right)^2 \right\} (V_T + V_Y) \end{aligned} \tag{37}$$

where $K_h(\sigma)$ and $K_e(T_{\circ C})$ can be acquired by fitting the iron loss curves.

III. Analysis of Multiphysics Factors

A. *Experimental System Establishment*

An IPMSM prototype for driving EVs is tested to verify the proposed iron loss predictive model. The stator and rotor structures, as well as the setup and operating principles of the integrated experimental platform are illustrated in Fig. 5 [4]. The specifications are listed in Table I. The control and measuring equipment including the control and drive circuits, the dynamometer, and the dynamic torque/speed sensors are mounted on the counter-towing experimental platform. Besides, a DC power supply is utilized for providing the desired DC power to the text motor, an upper computer is used for writing the control program, an electrical control cabinet is employed to collect speed & torque data and simulate different load conditions, while an oscilloscope is applied for the waveform recording and data processing. Moreover, the prototype is also simulated by a 2D time-stepping FEM in ANSYS, as shown in Fig. 6.

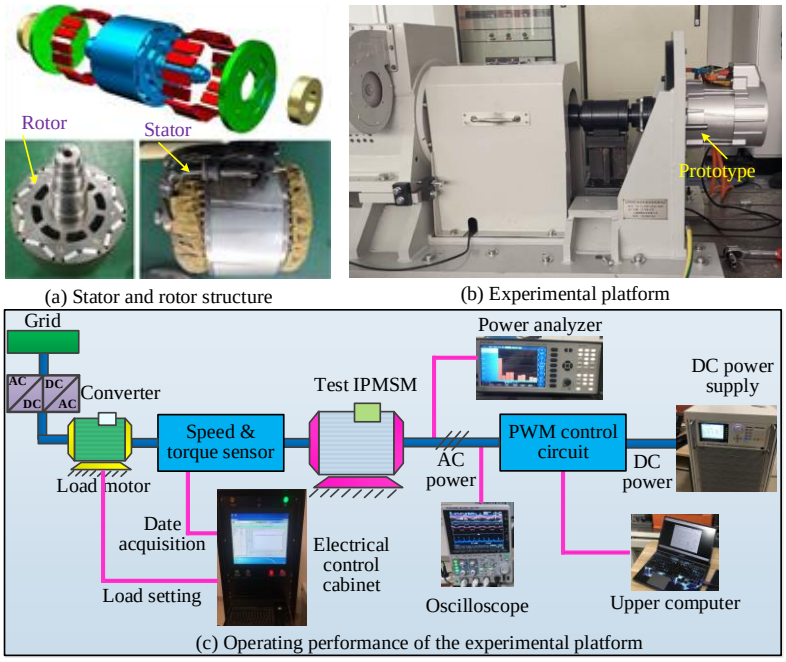

Fig. 5. Setup and operating principles of the integrated experimental platform [4].

TABLE I
SPECIFICATIONS OF THE IPMSM USED IN EVS

Items	Values	Items	Values
No. of poles	8	Core material	35WW360
No. of slots	48	Core length	108 mm
No. of phases	3	Stator outer diameter	196 mm
Magnets per pole	2	Stator inner diameter	135 mm
Rated power	20 kW	Rotor outer diameter	134 mm
Rated speed	3600 rpm	Air-gap length	0.5 mm
Maximum power	40 kW	Tooth width	6.35 mm
Maximum speed	5500 rpm	Magnet width	19.5 mm
Rated torque	53 Nm	V-shaped angle	145°
Maximum torque	180 Nm	Phase resistance	0.0052 Ω

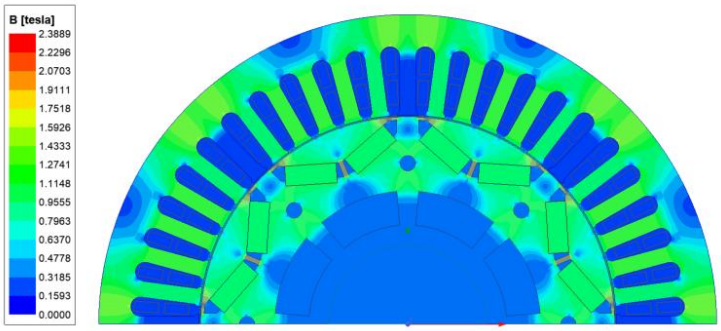

Fig. 6. 2D FEM model of the IPMSM.

B. *Effects of Harmonics*

For the inverter-fed IPMSM, there are various harmonic components in the output voltage of PWM inverter [31], [32]. But the voltage or voltage harmonics would not directly generate the iron loss that is caused by the changing of magnetic flux density, since the magnetic field is generated by current according to Ampere's Law [32]. In this case, when the motor is driven at 3000 rpm under load condition, the output current waveform of inverter is obtained. Fig. 7 shows the carrier harmonic characteristics with the developed SPWM strategy based on sampling method [32]. As shown, the current waveform mainly contains the 5th, 7th, 11th, 13th and 19th harmonics, which are more than 10% of the fundamental component.

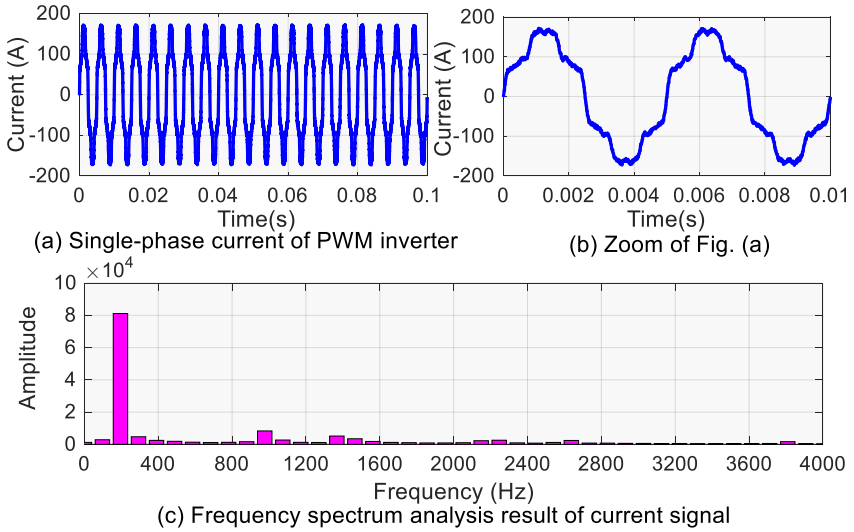

Fig. 7. Output current waveform of PWM inverter.

In order to show the harmonic effects during iron loss calculation, the air-gap flux density waveforms with PWM current input are also obtained by taking advantage of the established 2D time-stepping FEA model, as shown in Fig. 8. The magnitudes of the fundamental component and individual harmonics were calculated by using the discrete Fourier transform method, and the combined simulations of Simplorer and ANSYS can be utilized to obtain the airgap flux density with the sinusoidal and PWM supplies. It is worth mentioning that the magnetic field finite element analysis is conducted with the excitations of both the stator currents and rotor magnets. As seen from Fig. 8, because of the current harmonics, the flux waveforms are distorted significantly.

C. Effects of Multiphysics Factors

Apart from the PWM harmonics, the temperature and stress field distributions of the stator in the IPMSM prototype are also analyzed via FEM. To estimate the temperature distribution, it is assumed that there is no heat exchange between stator and rotor while the mechanical compressive stress in the stator is calculated based on the theory of thick-walled cylinders of elastic mechanics [33]. The FEM maps of temperature and stress field distributions at rated operating point are illustrated in Fig. 9. It can be seen that the maximum temperature happens at the top of the tooth region and reaches 89 ℃, while the maximum stress exists at the bottom of stator slot and can be up to 90 MPa. The average temperature of the stator is about 60 ℃ and the average stress is around 50 Mpa. In order to precisely predict the iron loss of electrical motors based on the proposed approaches, the data of the silicon steel sheets loss under different working conditions are measured by using the monolithic measurement method in the built 2-D magnetic property testing system, then utilized to calculate the loss coefficients at different working points (speed range of 500-5500 rpm with the interval of 500 rpm, temperature range of 30-100 ℃ with the interval of 10 ℃, stress range of 20-90 MPa with the interval of 10 Mpa) through the Lsqcurve fit in Matlab software. Finally, when the stress values are determined, the 3D maps of loss coefficients shown in Figs. 10 (a) and (b) can be obtained with the measured data under different working speeds and temperatures. When the temperature values are determined, the 3D maps of loss coefficients under different working speeds and stresses shown in Figs. 10 (c) and (d) can also be fitted.

The predicted loss coefficients, considering the coupling effects of multiphysics factors, can thus be substituted into (37) for iron loss calculation. As shown, when the temperature increases, the eddy current loss coefficient decreases significantly (about 35%) while the hysteresis loss coefficient varies slightly (only around 2%). Meanwhile, K_h increases by 15% with the increase of stress, while K_e varies by only 1% regardless of the stress.

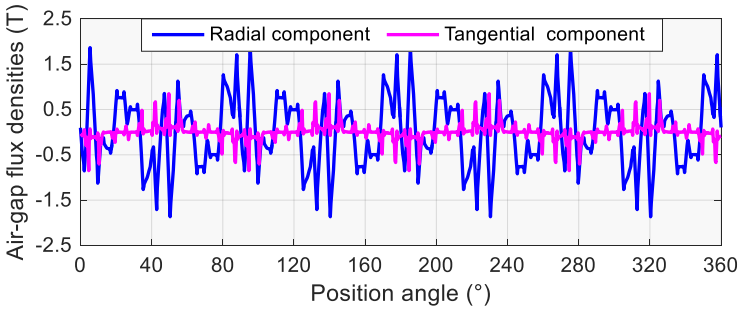

Fig. 8. Predicted air-gap flux density waveforms.

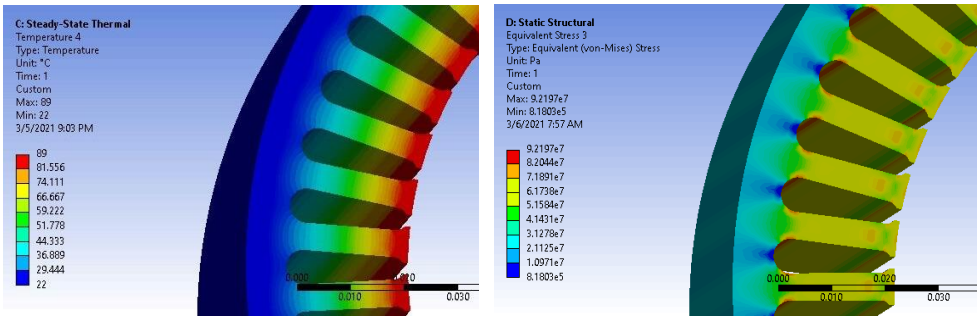

(a) Temperature field distributions of stator (b) Stress field distributions of stator

Fig. 9. FEM maps of temperature and stress field distributions.

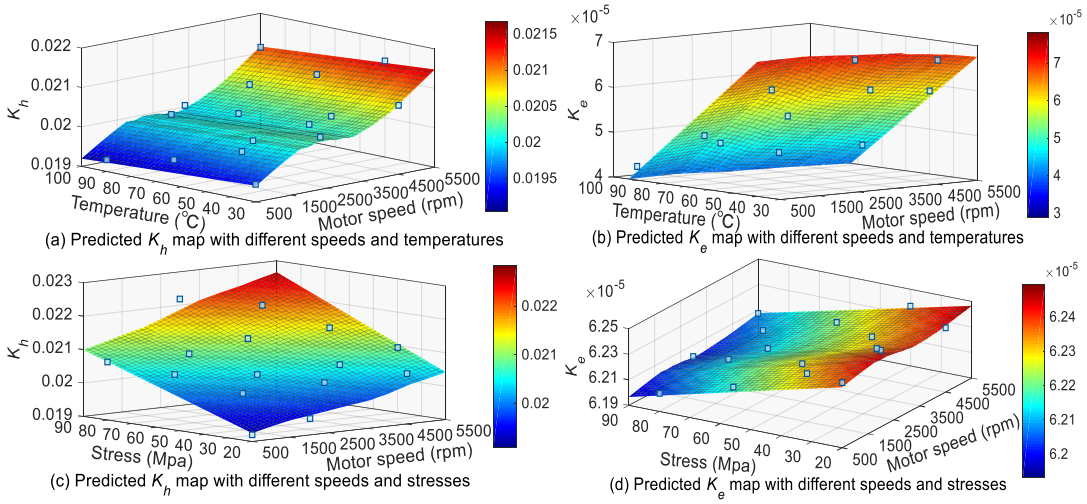

(a) Predicted K_h map with different speeds and temperatures

(b) Predicted K_e map with different speeds and temperatures

(c) Predicted K_h map with different speeds and stresses

(d) Predicted K_e map with different speeds and stresses

Fig. 10. Predicted 3D maps of loss coefficients.

IV. Analysis of Multiphysics Factors

A. No-load condition

To verify the superiority in the prediction accuracy and the computational burden of the proposed iron loss analytical model, the iron loss of the IPMSM prototype under no-load condition is predicted by using the proposed model, then compared with the values obtained by the Bertotti separation analytical model and numerical FEM. In the calculation, $\alpha = 2$ and $C_N = 0.41$ hold. Meanwhile, for better comparison, the magnetic-effect, temperature-effect, and stress-effect on the loss coefficients are considered in both the proposed model and the numerical FEM, while these factors were not given into considerations in the Bertotti model.

Three conditions are set for case studies, namely, 'case (i): the temperature is fixed at 30 ℃, and stress at 90 MPa, case (ii): the temperature is fixed at 30 ℃, and stress at 20 MPa, and case (iii): the temperature is fixed at 100 ℃, and stress at 20 MPa'. Figs. 11-13 illustrate the iron losses obtained by the three models at different motor speeds in the range of 500 - 5500 rpm, under the operating conditions of cases (i), (ii) and (iii), respectively. Since the speed ripples are relatively small, more attentions are paid to the iron loss performance under static operating state and the speed harmonics or ripples are neglected in the case studies. As seen from Figs. 11-13, the stator iron loss has a significant upward increase along with the speed increase. Meanwhile, the temperature rise and mechanical stress have non-ignorable impacts on the iron loss, which would be fully analyzed later.

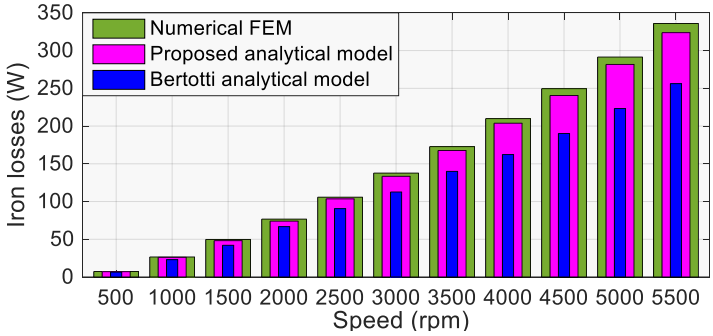

Fig. 11. Comparative results of iron losses under case (i).

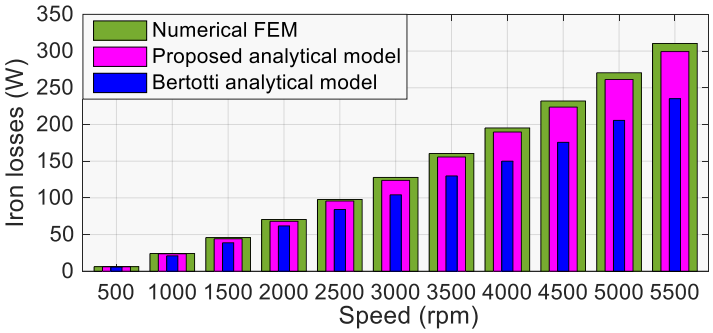

Fig. 12. Comparative results of iron losses under case (ii).

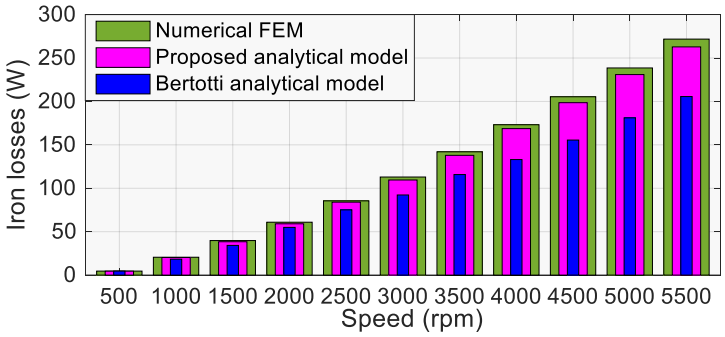

Fig. 13. Comparative results of iron losses under case (iii).

TABLE II
ERROR ANALYSIS OF FIGS. 11, 12 AND 13

Items	EM_{11}	EA_{11}	EM_{12}	EA_{12}	EM_{13}	EA_{13}
Bertotti	23.68%	17.90%	24.27%	17.85%	24.34%	16.35%
Proposed	3.53%	2.95%	3.59%	3.03%	3.30%	2.73%

The error analysis between the analytical models and FEM, corresponding to Figs. 11-13, is presented in Table II, where EM_i and EA_i (i = 11, 12, 13) represent the maximum and absolute average errors of iron losses which are relative to Figs. 11, 12 and 13, respectively. As shown, under different working modes, the maximum errors between the iron loss calculated by the proposed approach and the values obtained by FEM are 3.53%, 3.59% and 3.30% for cases (i), (ii) and (iii), respectively, while the absolute average errors are all within 3.03% in spite of the temperature and stress. For Bertotti method, the maximum errors exceed 23.68% and the absolute average errors are all greater than 16.35%. Moreover, the proposed method took only a few minutes for iron loss calculation, while the FEM required about 56 minutes. The results illustrate very well the superior performance of the proposed models in accuracy and conciseness of iron loss prediction with no-load condition.

B. Load condition

Although the results under no-load condition indicate that the proposed model is efficient for the iron loss prediction of IPMSMs, the PWM carrier harmonics are not fully considered. For better verification, the measured iron losses of the prototype are compared with those predicted by the FEM, the method considering PWM and slotting harmonics [25], and the proposed model in terms of different input phase currents of 64 A, 180 A, 285 A and 588 A with the average temperature and stress. The PWM effects are considered in all the prediction methods, while the coupling effects of temperature and stress on the loss coefficients are only involved in the proposed methods to clearly verify the contributions of this work. Taking advantage of the simple structure, fast dynamic response and strong robustness, the field-oriented control (FOC) strategy [34] is used to carry out the experiments, aiming to achieve the maximum torque per ampere. It is worth mentioning that the iron loss of the prototype cannot be measured directly with the experimental platform. The IPMSM mainly contains four kinds of losses, i.e. the iron loss, copper loss, mechanical loss and stray loss. The copper loss can be calculated based on the phase current and winding resistance. The mechanical losses are determined through a so-called dummy rotor method which was successfully employed in our publication [35]. In this scheme, the motor rotor is replaced by a wooden rotor with a similar shape as the real rotor. Assuming that the mechanical losses with the two rotors are the same under the same speed, then the mechanical loss of the test motor at various speeds can be obtained as the input power of the drive motor since there is no magnetic field, induced voltage and current in the stator, i.e. no iron loss or copper loss. The stray loss is empirically assumed to be 1% of the output power [5]. Thus, the iron loss of the prototype can be calculated by

$$P_{ironM} = P_{inputM} - P_{copperM} - P_{mechM} - 1.01P_{outputM} \tag{38}$$

where P_{totalM} and $P_{outputM}$ are the measured input and output powers, while $P_{copperM}$ and $P_{outputM}$ are the derived copper loss and stray loss based on the experimental data.

To make the mechanical loss data more convincing, we carried out experiments to measure the mechanical losses at every speed for three times, and determined the mechanical losses by the means. Fig. 14 shows the measured mechanical loss curve with motor speeds. Then, the comparative experimental results are obtained with (38) and illustrated in Fig. 15. The error analysis between the measured iron losses and the predicted values is presented Table III, where EM_j and EA_j (j = 64, 180, 285 and 588) represent the maximum and absolute average errors of iron loss which are relative to those measured by the experimental platform under 64 A, 180 A, 285 A and 588 A phase currents, respectively.

As shown in Table III, with different phase current inputs, the maximum and absolute average errors of the measured iron losses and the values calculated by the proposed model are less than 5.85% and 4.71%, respectively, which are around 45% of the errors for the numerical FEM. The computational times are also much shorter. Although the method in [25] takes little computational time as the propose models, the maximum and absolute average errors compared with the measured values are bigger than 11.62% and 11.41%, respectively, regardless of the current inputs. Owing to the loss separation error and the unaccountable influence of temperature and stress, there is a deviation of about 10% between the iron losses obtained by the FEM and experiment measurement. Moreover, taking advantage of considering the multiphysics factors, especially the PWM harmonics, the proposed model has better

prediction accuracy than FEM. All the results show the satisfactory performances of the proposed iron loss model under load conditions. The visible relationships between these multiphysics factors and the final iron loss are also revealed through the improved iron loss prediction model.

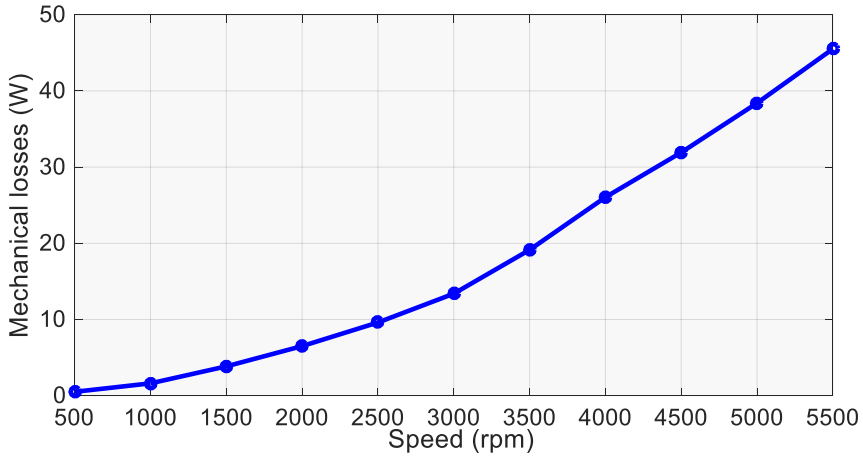

Fig. 14. Measurement results of mechanical losses

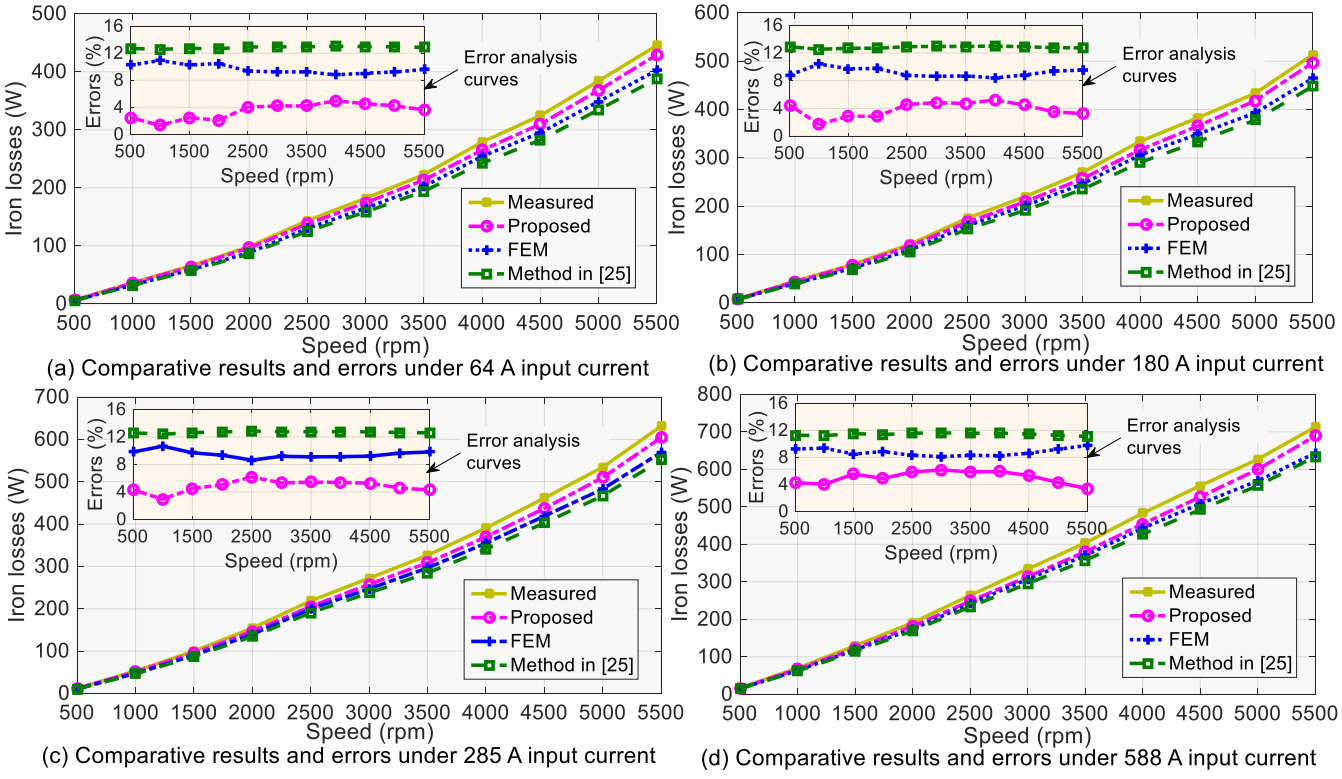

Fig. 15. Comparative results of iron losses under different working speeds and phase current conditions

TABLE III
DATA ANALYSIS OF FIG. 14

Items	FEM	Proposed	Method in [25]	Items	FEM	Proposed	Method in [25]
EM_{64}	10.91%	4.95%	13.03%	EM_{285}	10.66%	5.39%	12.87%
EA_{64}	9.61%	3.56%	12.84%	EA_{285}	9.44%	3.89%	12.68%
EM_{180}	10.39%	5.22%	12.99%	EM_{588}	9.37%	5.85%	11.62%
EA_{180}	9.21%	3.80%	12.81%	EA_{588}	8.72%	4.71%	11.41%

C. Effects of the Multiphysics Factors

In order to illustrate the coupling effects of multiphysics factors, the control variable method is utilized for analyzing the single temperature-effect, and stress-effect on the final iron loss value of the IPMSM. Based on the verifications outlined above, the iron losses under varying temperatures and stresses are calculated by using the proposed model and given in Fig. 16. The current is fixed at 180 A and motor speed at 3000 rpm.

As shown, the iron loss decreases by a range of 15.20% when the temperature increases from 30 ℃ to 100 ℃, while the iron loss value increases by 10.03% with the expansion of stress from 20 MPa to 90 MPa. Results indicates that the loss coefficients are not only affected by the frequency but also strongly related to the temperature rise and mechanical stress.

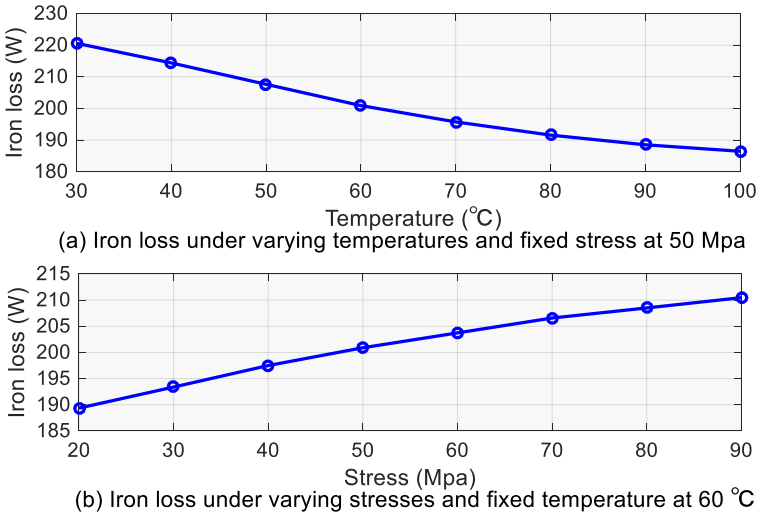

Fig. 16. Iron losses under varying temperatures and stresses.

V. CONCLUSIONS

Aiming at the coupling effects of multiphysics factors, an improved iron loss prediction model for IPMSMs, used in EVs, is proposed, which accounts for the slotting harmonics, PWM harmonics, temperature and stress influences. The accuracy and superiority of the proposed model is verified by comparing its results with the results obtained by experimental testing, FEM, and the Bertotti methods on an IPMSM prototype. The main conclusions are as follows.

i) The proposed model has good performances for iron loss prediction. Under no-load condition, a comparison with the FEM results shows that the maximum and absolute average errors are less than 3.59% and 3.03%, respectively, in the case of varying motor operating speeds, temperatures and stresses. Under load conditions, the comparison between the iron loss results of experimental measurement and theoretical prediction by the proposed model also shows a very small error that accounts for only 45% of the errors for the numerical FEM. Moreover, the computational cost can also be greatly reduced.

ii) The iron loss is affected by the slotting harmonics, PWM carrier harmonics, temperature rise, and mechanical stress. Specifically, the eddy current loss coefficient is mainly related to the thermal field, and the hysteresis loss coefficient has a strong dependency on the stress field. Furthermore, the iron loss increases when the stress increases, while the iron loss reduces when the temperature rises.

The results of this paper may provide useful references for not only the accurate iron loss prediction but also multiphysics design optimization of PM motors. Future works including the validation works of different types PM motors under extreme working conditions can be conducted to improve the proposed iron loss prediction model in adaptability.

REFERENCES

[1] X. Sun, Z. Shi, Y. Cai, G. Lei, Y. Guo, and J. Zhu, "Driving cycle oriented design optimization of a permanent magnet hub motor drive system for a four-wheel-drive electric vehicle," *IEEE Trans. Transp. Electr.*, vol. 6, no. 3, pp. 1115-1125, Sep. 2020.

[2] G. Lei, T. Wang, J. Zhu, Y. Guo, and S. Wang, "System-level design optimization method for electrical drive systems-robust approach," *IEEE Trans. Ind. Electron.*, vol. 62, no. 8, pp. 4702-4713, Aug. 2015.

[3] W. Wang, P. Zheng, M. Wang, Y. Liu, Z. Fu, and Y. Sui, "Demagnetization and permanent-magnet minimization analyses of less rare earth interior permanent-magnet synchronous machines used for electric vehicles," *IEEE Trans. Magn.*, vol. 54, no. 11, pp. 1-5, Nov. 2018.

[4] K. D. Hoang, and H. K. A. Aorith, "Online control of IPMSM drives for traction applications considering machine parameter and inverter nonlinearities," *IEEE Trans. Transp. Electr.*, vol. 1, no. 4, pp. 312-325, Dec. 2015.

[5] G. Lei, J. Zhu, and Y. Guo, Multidisciplinary Design Optimization Methods for Electrical Machines and Drive Systems, Berlin, Heidelberg: Springer Berlin / Heidelberg, 2016.

[6] Y. Oda, H. Toda, N. Shiga, S. Kasai, and T. Hiratani, "Effect of Si content on iron loss of electrical steel sheet under compressive stress," *IEEE Trans. Magn.*, vol. 50, no. 4, pp. 1-4, Apr. 2014.

[7] D. Zhang, T. Liu, H. Zhao, and T. Wu, "An analytical iron loss calculation model of inverter-fed induction motors considering supply and slot harmonics," *IEEE Trans. Ind. Electron.*, vol. 66, no. 12, pp. 9194-9204, Dec. 2019.

[8] G. Bertotti, A. Canova, M. Chiampi, D. Chiarabaglio, F. Fiorillo, and A. M. Rietto, "Core loss prediction combining physical models with numerical field analysis," *J. Magn. Magn. Mater*., vol. 133, pp. 647–650, 1994.

[9] K. Yamazaki, Y. Fukushima, and M. Sato, "Loss analysis of permanent-magnet motors with concentrated windings-variation of magnet eddy-current loss due to stator and rotor shapes," *IEEE Trans. Ind. Appl.*, vol. 45, no. 4, pp. 1334-1342, Jul.-Aug. 2009.

[10] F. Henrotte, S. Steentjes, K. Hameyer, and C. Geuzaine, "Iron loss calculation in steel laminations at high frequencies," *IEEE Trans. Magn.*, vol. 50, no. 2, pp. 333-336, Feb. 2014.

[11] O. Payza, Y. Demir, and M. Aydin, "Investigation of losses for a concentrated winding high-speed permanent magnet-assisted synchronous reluctance motor for washing machine application," *IEEE Trans. Magn.*, vol. 54, no. 11, pp. 1-5, Nov. 2018.

[12] X. Chen, J. Wang, B. Sen, P. Lazari, and T. Sun, "A high-fidelity and computationally efficient model for interior permanent-magnet machines considering the magnetic saturation, spatial harmonics, and iron loss effect," *IEEE Trans. Ind. Electron.*, vol. 62, no. 7, pp. 4044-4055, Jul. 2015.

[13] B. Scheerlinck, H. De Gersem, and P. Sergeant, "Reducing losses due to fringing flux in an axial-flux permanent-magnet synchronous machine," IEEE Trans. Magn., vol. 52, no. 10, pp. 1-8, Oct. 2016.

[14] I. Suehiro, T. Mifune, T. Matsuo, J. Kitao, T. Komatsu, and M. Nakano, "Ladder circuit modeling of dynamic hysteretic property representing excess eddy-current loss," *IEEE Trans. Magn.*, vol. 54, no. 3, pp. 1-4, Mar. 2018.

[15] A. Hemeida, A. Lehikoinen, P. Rasilo, H. Vansompel, A. Belahcen, A. Arkkio, and P. Sergeant, "A simple and efficient quasi-3D magnetic equivalent circuit for surface axial flux permanent magnet synchronous machines," *IEEE Trans. Ind. Electron.*, vol. 66, no. 11, pp. 8318-8333, Nov. 2019.

[16] A. R. Tariq, C. E. Nino-Baron, and E. G. Strangas, "Iron and magnet losses and torque calculation of interior permanent magnet synchronous machines using magnetic equivalent circuit," *IEEE Trans. Magn.*, vol. 46, no. 12, pp. 4073-4080, Dec. 2010.

[17] H. W. Derbas, J. M. Williams, and S. D. Pekarek, "A comparison of nodal- and mesh-based magnetic equivalent circuit models," *IEEE Trans. Energy Convers.*, vol. 24, no. 2, pp. 388-396, Jun. 2009.

[18] P. Liang, F. Chai, and Y. Wang, "Analytical prediction of no-load stator iron losses in spoke-type permanent-magnet synchronous machines," *IEEE Trans. Energy Convers.*, vol. 33, no. 1, pp. 252-259, Mar. 2018.

[19] P. Liang, Y. Tang, F. Chai, K. Shen, and W. Liu, "Calculation of the iron losses in a spoke-type permanent magnet synchronous in-wheel motor for electric vehicles by utilizing the Bertotti model," *IEEE Trans. Magn.*, vol. 55, no. 7, pp. 1-7, Jul. 2019.

[20] Q. Li, T. Fan, and X. Wen, "Characterization of iron loss for integral-slot interior permanent magnet synchronous machine during flux weakening," *IEEE Trans. Magn.*, vol. 53, no. 5, pp. 1-8, May 2017.

[21] W. Q. Chu, Z. Zhu, X. Liu, D. A. Stone, and M. P. Foster, "Iron loss calculation in permanent magnet machines under unconventional operations," *IEEE Trans. Magn.*, vol. 50, no. 11, pp. 1-4, Nov. 2014.

[22] Y. Miyama, M. Hazeyama, S. Hanioka, N. Watanabe, A. Daikoku, and M. Inoue, "PWM carrier harmonic iron loss reduction technique of permanent-magnet motors for electric vehicles," *IEEE Trans. Ind. Electron.*, vol. 52, no. 4, pp. 2865-2871, Jul.-Aug. 2016.

[23] F. Chai, P. Liang, Y. Pei, and S. Cheng, "Magnet shape optimization of surface-mounted permanent-magnet motors to reduce harmonic iron losses," *IEEE Trans. Magn.*, vol. 52, no. 7, pp. 1-4, Jul. 2016.

[24] L. Yu, Z. Zhang, Z. Bian, D. Gerada, and C. Gerada, "Dual-pulse mode control of a high-speed doubly salient electromagnetic machine for loss reduction and speed range extension," *IEEE Trans. Ind. Electron.*, vol. 67, no. 6, pp. 4391-4401, Jun. 2020.

[25] S. Zhu, J. Dong, Y. Li, and W. Hua, "Fast calculation of carrier harmonic iron losses caused by pulse width modulation in interior permanent magnet synchronous motors," *IET Electr. Power App.*, vol. 14, no. 7, pp. 1163-1176, May 2020.

[26] C. Zhang, L. Chen, X. Wang, and R. Tang, "Loss calculation and thermal analysis for high-speed permanent magnet synchronous machines," *IEEE Access*, vol. 8, pp. 92627-92636, May 2020.

[27] D. Miyagi, Y. Aoki, and N. Takahashi, "Effect of compressive stress in thickness direction on iron losses of non-oriented electrical steel sheet," *IEEE Trans. Magn.*, vol. 46, no. 6, pp. 2040-2043, Jun. 2010.

[28] S. Xue, J. Feng, S. Guo, J. Peng, and Z. Q. Zhu, "A new iron loss model for temperature dependencies of hysteresis and eddy current losses in electrical machines," *IEEE Trans. Magn.*, vol. 54, no. 1, pp. 1-10, Jan. 2018.
[29] J. Lavers, P. Biringer, and H. Hollitscher, "Estimation of core losses when the flux waveform contains the fundamental plus a single odd harmonic component," *IEEE Trans. Magn.*, vol. 13, no. 5, pp. 1128-1130, Sep. 1977.
[30] W. Roshen, "Iron loss model for permanent-magnet synchronous motors," *IEEE Trans. Magn..*, vol. 43, no. 8, pp. 3428-3434, Aug. 2007.
[31] H. Qamar, H. Qamar and R. Ayyanar, "Performance analysis and experimental validation of 240°-clamped space vector PWM to minimize common mode voltage and leakage current in EV/HEV traction drives," *IEEE Trans. Transp. Electr.*, vol. 8, no. 1, pp. 196-208, Mar. 2022.
[32] D. G. Holmes, and T. A. Lipo. *Pulse Width Modulation for Power Converters: Principles and Practice*. USA: Wiley & Sons, 2003.
[33] T. Y. Wang, F. Q. Wen, and F. G. Zhang, "Analysis of multi-field coupling strength for MW high-speed permanent magnet machine," *Trans. China Electrotech. Soc.*, vol. 33, no. 19, pp. 4508–4516, Oct. 2018.
[34] T. Sun, J. Wang, C. Jia, and L. Peng, "Integration of FOC with DFVC for interior permanent magnet synchronous machine drives," *IEEE Access*, vol. 8, pp. 97935-97945, May 2020.
[35] Y. Guo, J. Zhu, H. Lu, Z. Lin, and Y. Li, "Core loss calculation for soft magnetic composite electrical machines," *IEEE Trans. Magn.*, vol. 48, no. 11, pp. 3112-3115, Nov. 2012.

Lin Liu (S'20) received the B.E. degree in automation and the M.E. degree in control and computer engineering from North China Electric Power University, Beijing, China, in 2016 and 2019, respectively. From 2017 to 2019, she was sponsored to conduct her study at the South Ural State University, Chelyabinsk, Russia, where she received the second M.E. degree in electrical engineering. She is currently working toward a Ph.D. degree in electrical and data engineering with University of Technology Sydney, Sydney, Australia. She is also working as the WiE affinity vice-chairwoman for the UTS-IEEE student branch. Her main research area includes the design optimization of electrical drive systems as well as the data analysis and mining for condition monitoring of energy and power systems.

Xin Ba received the B.E. degree from the Lanzhou University of Technology, Lanzhou, China, in 2011, the M.E. degree from Beijing Information Science and Technology University, Beijing, China, in 2015, and the Ph.D. degree from the Beijing Institute of Technology, China, in 2020, all in mechanical engineering. She is currently pursuing the Ph.D. degree in electrical engineering with the School of Electrical and Data Engineering, University of Technology Sydney (UTS), Australia. She is also a Postdoctoral Fellow with the School of Mechanical Engineering, Beijing Institute of Technology, China. Her research interests include measurement and modeling of magnetic materials properties, and numerical analysis of electromagnetic field.

Youguang Guo (S'02-M'05-SM'06) received the B.E. degree from Huazhong University of Science and Technology, China in 1985, the M.E. degree from Zhejiang University, China in 1988, and the Ph.D. degree from University of Technology Sydney (UTS), Australia in 2004, all in electrical engineering. He is currently a professor at the School of Electrical and Data Engineering, UTS. His research fields include measurement and modeling of properties of magnetic materials, numerical analysis of electromagnetic field, electrical machine design optimization, power electronic drives and control.

Gang Lei (M'14) received the B.S. degree in Mathematics from Huanggang Normal University, China, in 2003, the M.S. degree in Mathematics and Ph.D. degree in Electrical Engineering from Huazhong University of Science and Technology, China, in 2006 and 2009, respectively. He is currently a senior lecturer at the School of Electrical and Data Engineering, University of Technology Sydney (UTS), Australia. His current research interests include electrical machines and systems, multidisciplinary design optimization, industrial big data and cloud computing techniques.

Xiaodong Sun (SM) received the B.Sc. degree in electrical engineering and the M.Sc. and Ph.D. degrees in control engineering from Jiangsu University, China, in 2004, 2008, and 2011, respectively. Since 2004, he has been with Jiangsu University, where he is currently a professor in vehicle engineering with the Automotive Engineering Research Institute. His current teaching and research interests include electrified vehicles, electrical machines, electrical drives, and energy management. He is an Editor of the IEEE Transactions on Energy Conversion.

Jianguo Zhu (S'93–M'96–SM'03) received the B.E. degree from Jiangsu Institute of Technology, China, in 1982, the M.E. degree from Shanghai University of Technology, China, in 1987, and the Ph.D. degree from the University of Technology, Sydney (UTS), Australia, in 1995, all in electrical engineering. He is currently a professor (head of school) in Electrical Engineering at the University of Sydney, Australia. His research interests include electromagnetics, magnetic properties of materials, electrical machines and drives, power electronics, and green energy systems.